The effect of Mach number on unstable disturbances in shock/boundary-layer interactions

Y. Yao[a)]
Faculty of Engineering, Kingston University, London SW15 3DW, United Kingdom

L. Krishnan, N. D. Sandham, and G. T. Roberts
School of Engineering Sciences, University of Southampton, Southampton SO17 1BJ, United Kingdom

(Received 21 July 2006; accepted 5 March 2007; published online 10 May 2007)

The effect of Mach number on the growth of unstable disturbances in a boundary layer undergoing a strong interaction with an impinging oblique shock wave is studied by direct numerical simulation and linear stability theory (LST). To reduce the number of independent parameters, test cases are arranged so that both the interaction location Reynolds number (based on the distance from the plate leading edge to the shock impingement location for a corresponding inviscid flow) and the separation bubble length Reynolds number are held fixed. Small-amplitude disturbances are introduced via both white-noise and harmonic forcing and, after verification that the disturbances are convective in nature, linear growth rates are extracted from the simulations for comparison with parallel flow LST and solutions of the parabolized stability equations (PSE). At Mach 2.0, the oblique modes are dominant and consistent results are obtained from simulation and theory. At Mach 4.5 and Mach 6.85, the linear Navier-Stokes results show large reductions in disturbance energy at the point where the shock impinges on the top of the separated shear layer. The most unstable second mode has only weak growth over the bubble region, which instead shows significant growth of streamwise structures. The two higher Mach number cases are not well predicted by parallel flow LST, which gives frequencies and spanwise wavenumbers that are significantly different from the simulations. The PSE approach leads to good qualitative predictions of the dominant frequency and wavenumber at Mach 2.0 and 4.5, but suffers from reduced accuracy in the region immediately after the shock impingement. Three-dimensional Navier-Stokes simulations are used to demonstrate that at finite amplitudes the flow structures undergo a nonlinear breakdown to turbulence. This breakdown is enhanced when the oblique-mode disturbances are supplemented with unstable Mack modes. © *2007 American Institute of Physics*.
[DOI: 10.1063/1.2720831]

I. INTRODUCTION

Shock/boundary-layer interaction (SBLI) phenomena are common occurrences in transonic, supersonic, and hypersonic flows. They often result in boundary-layer separation, which can result in reduced performance (e.g., in engine inlets), increased drag (e.g., on airfoils and other aerodynamic surfaces) and, especially in the hypersonic case, enhanced surface heating. Consequently, these flow phenomena have been investigated extensively, for a variety of geometric configurations and over a broad range of Mach numbers and Reynolds numbers. Several comprehensive reviews of the work have been published (Adamson and Messiter,[1] Delery,[2] Dolling,[3] Knight *et al.*[4]).

Although SBLI occurs in various geometries, a simple configuration that has often been studied and includes all of the relevant physical features is that of an oblique shock wave impinging on a flat plate over which a boundary layer is developing. In principle, if the plate is wide enough, the resultant flow field will be essentially two dimensional (2D) in nature. Figure 1 gives a schematic of such a configuration. The Mach number upstream of the interaction is denoted by M_1, and regions (1), (2), and (3) refer to the flow upstream of the impinging shock after the initial shock and after the reflected shock, respectively. The impinging shock angle is denoted by β_1 and the strength of the interaction is characterized by the overall pressure ratio p_3/p_1, which is governed by M_1 and β_1. As the shock wave impinges on the boundary layer, the latter at first thickens due to the imposed adverse pressure gradient. If the impinging shock is sufficiently strong, the boundary layer will separate and then later reattach, forming a closed separation bubble. The separation and reattachment points are denoted by x_s and x_r in Fig. 1, and the length of the bubble is defined as $L_B=x_r-x_s$. During the interaction, further compression and expansion waves are created, caused by the deflection of the inviscid flow field resulting from the boundary layer separation. The compression waves may merge to form additional shocks, typically near the separation and reattachment regions.

Most previous studies in SBLI have been concerned with fully developed turbulent boundary layers. One aspect of SBLI that is receiving significant attention currently is the influence of boundary-layer transition. Boundary-layer transition itself is a process that, despite extensive study over

[a)]Telephone: +44 (0)208 5477822. Fax: +44 (0)208 5477992. Electronic mail: y.yao@kingston.ac.uk

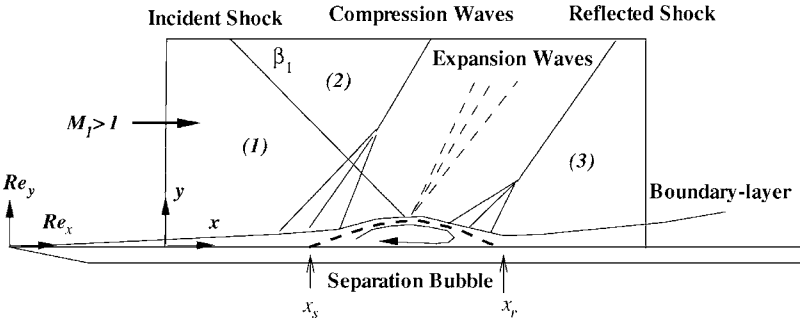

FIG. 1. Schematic view of an oblique shock wave impinging on a flat plate boundary layer.

many years, is not yet fully understood. It is generally accepted that, at a sufficiently high Reynolds number, disturbances (either inherent in the flow or created by some external means) become unstable and provoke transition from laminar to turbulent flow in the boundary layer. However, in addition to the Reynolds number, many other factors also influence this process, including the level of acoustic free-stream turbulence, wall roughness, wall temperature, and the Mach number of the flow (see Saric *et al.*,[5] Ma and Zhong[6]).

Results from linear stability analysis (LSA) of compressible flows are reported in detail in Mack[7] for attached boundary layers. At low Mach numbers ($\leqslant 0.3$), the Tollmien-Schlichting (first mode) waves are the most unstable disturbances beyond a critical Reynolds number. As the Mach number increases, additional "Mack" modes (second mode, third mode, etc.) of instability appear, and at high Mach numbers these are the most unstable disturbances. Flow stability results in SBLI at $M_1=4.8$, focusing on the second-mode instabilities, are reported in Pagella *et al.*[8] for a flat plate boundary layer and at $M_1=5.373$ in Balakumar *et al.*[9] for a compression corner flow.

The parabolized stability equations (PSE; see Herbert,[10] Hein *et al.*[11]) approach improves on the e^n method (Arnal and Casalis,[12] Stock[13]) by including nonparallel terms and allowing for the streamwise evolution of disturbance shape functions. The method is applicable to convectively unstable flow but, although widely used for transition prediction on wings, it does not appear to have been applied to SBLI until now.

Direct numerical simulation (DNS) has been applied extensively to study transition in low-speed flows (e.g., Kleiser and Zang[14]) and a few applications have been made to SBLI flows. Pagella *et al.*[8] created a 2D SBLI by impinging an oblique shock wave on a flat plate boundary layer at a Mach number of 4.8. In this work, the response of the initially laminar boundary layer to artificially introduced small-amplitude disturbances was investigated and the results compared well with those of linear stability theory. This work was later extended to the case of a 2D compression ramp flow, also at Mach 4.8 (Pagella *et al.*[15]), showing that, when the impinging shock and the shock created by the compression ramp have the same strength, the characteristics of SBLI were identical (validating the so-called *free interaction* concept originated by Chapman *et al.*[16]). This latter work also demonstrated that the response to small-amplitude disturbances was practically identical. Compression corner flows at $M_1=5.373$ were also considered by Balakumar *et al.*,[9] who showed that the second-mode disturbances were not significantly amplified over the separation bubble. In a later study of the same compression corner flow, Zhao and Balakumar[17] showed that a (0,2) mode arising from nonlinear interactions led to an oblique type of breakdown. Nonlinear disturbances and breakdown to turbulence in a flat plate boundary layer with an impinging shock were considered by Teramoto[18] using large-eddy simulation at Mach 2.0. At a high pressure ratio ($p_3/p_1=1.91$), it was found that transition occurred even at zero free-stream turbulence level. This indicates the presence of absolute instability of the laminar base flow, although the resolutions used were not sufficient to achieve grid-independent results.

In the present study, we revisit the case of a shock wave impinging on a flat plate with a 2D laminar base flow. Like Pagella *et al.*,[8] we initially examine the response of the laminar boundary layer to artificially introduced small-amplitude disturbances. On the other hand, we investigate the characteristics of SBLI and the boundary layer response over a range of upstream Mach numbers ($M_1=2.0$, 4.5, and 6.85), but keeping the impingement location Reynolds number constant. Because of the potentially large number of parameters that could influence the flow fields simulated, we examine the case of adiabatic flows with, additionally, a fixed Reynolds number based on the separation bubble length (i.e., Re_{L_B}). This, we feel, is the most logical procedure to isolate the effects of Mach number changes. Three-dimensional (3D) simulations use either white-noise forcing, such that the unstable modes could emerge naturally, or harmonic forcing at fixed frequencies and spanwise wavenumbers derived from LSA.

The paper includes a description of the overall methodology and the numerical techniques employed in this study. After some code validation cases are briefly described, the results of 2D simulations of the undisturbed SBLI flow field are presented. A local linear stability analysis is used to identify the most unstable modes in terms of frequency and spanwise wavenumber. From these we derive the appropriate computational domains for the subsequent three-dimensional simulations. The response of the boundary-layer disturbances is, where appropriate, compared with the results of linear stability theory, bearing in mind that the disturbances introduced are sufficiently weak for a linear response to be expected. Where differences in the results are identified, these are discussed in detail. The paper continues with a discussion of the effects of the nonparallel flow and Mach number

variation on the propensity of the separated boundary layer to undergo transition as a result of SBLI. Finally, 3D Navier-Stokes simulations using finite-amplitude disturbances are described. These were carried out to demonstrate the feasibility of the early-stage nonlinear breakdown and transition onset over the separation bubble.

II. NUMERICAL METHOD AND VALIDATIONS

A. Governing equations and discretization

The dimensionless 3D Navier-Stokes equations that govern the unsteady, compressible flows in Cartesian coordinates are written for density ρ, velocity components u_i, pressure p, and total energy E as

$$\frac{\partial \rho}{\partial t} + \frac{\partial \rho u_j}{\partial x_j} = 0, \tag{1}$$

$$\frac{\partial \rho u_i}{\partial t} + \frac{\partial \rho u_i u_j}{\partial x_j} = -\frac{\partial p}{\partial x_i} + \frac{1}{\mathrm{Re}} \frac{\partial \tau_{ij}}{\partial x_j}, \tag{2}$$

$$\frac{\partial E}{\partial t} + \frac{\partial (E+p) u_j}{\partial x_j} = \frac{\partial u_i \tau_{ij}}{\partial x_j} + \frac{1}{(\gamma - 1)\mathrm{Re}\,\mathrm{Pr}\,\mathrm{M}_1^2} \frac{\partial}{\partial x_j}\left(\mu \frac{\partial T}{\partial x_j}\right), \tag{3}$$

where the viscous stress tensor is given in terms of the viscosity μ by

$$\tau_{ij} = \mu\left(\frac{\partial u_j}{\partial x_i} + \frac{\partial u_i}{\partial x_j} - \frac{2}{3}\delta_{ij}\frac{\partial u_k}{\partial x_k}\right). \tag{4}$$

The temperature T is given by

$$T = \gamma(\gamma - 1)\mathrm{M}_1^2\left(\frac{E}{\rho} - \frac{1}{2}u_i u_i\right). \tag{5}$$

The ideal gas equation of state can be written as

$$p = (\gamma - 1)\left(E - \frac{1}{2}\rho u_i u_i\right) = \frac{1}{\gamma \mathrm{M}_1^2}\rho T. \tag{6}$$

The dimensionless parameters governing the flow are the Reynolds number $\mathrm{Re} = \rho_r^* u_r^* L_r^* / \mu_r^*$, the upstream Mach number $\mathrm{M}_1 = u_r^* / \sqrt{\gamma R^* T_r^*}$ (where R^* is the specific gas constant), the ratio of specific heats $\gamma = 1.4$, and the Prandtl number $\mathrm{Pr} = \mu_r^* c_p^* / k^*$, which is set to 0.72. The variation of the dynamic viscosity with temperature is accounted for by Sutherland's law $[\mu = T^{3/2}(1+c)/(T+c)$, with $c = 110.4/288]$. These parameters apply to undissociated air. In these expressions, the subscript "r" denotes a reference value and an asterisk represents dimensional variables. Further reference quantities will be discussed in Sec. IV.

This set of governing equations is solved using a stable high-order scheme. An "entropy splitting" approach is used to split the Euler terms into conservative and nonconservative parts. This method was originally proposed by Gerritsen and Olsson[19] and later applied by Yee *et al.*[20] and Sandham *et al.*[21] All the spatial discretizations are carried out using a fourth-order central-difference scheme, while the time integration uses a third-order Runge-Kutta method. A stable boundary scheme of Carpenter *et al.*,[22] along with a Laplacian formulation of the viscous and heat conduction terms, is used to prevent any odd-even decoupling associated with central-difference schemes. An artificial compression method variant of a standard total variation diminishing (TVD) family is used to capture flow discontinuities such as shock waves. The TVD filter is applied at the end of each full time step in the form of an additional numerical flux term (F) as

$$F_{j+1/2} = R_{j+1/2}\Phi_{j+1/2}\Psi_{j+1/2}, \tag{7}$$

where R is the right eigenvector matrix of the flux Jacobian from the Euler equations and Φ is defined by the TVD scheme of Yee *et al.*,[20] Ψ is the Ducros *et al.*[23] sensor, which is defined as

$$\Psi = \frac{(\boldsymbol{\nabla} \cdot \mathbf{V})^2}{(\boldsymbol{\nabla} \cdot \mathbf{V})^2 + (|\boldsymbol{\nabla} \times \mathbf{V}|)^2 + \epsilon}, \tag{8}$$

where $\mathbf{V}$ is the velocity vector and ϵ is machine zero.

B. Inflow and boundary conditions

The velocity and temperature profiles of a compressible laminar boundary layer are prescribed at the inlet plane of the computational domain. They are generated by a self-similar solution of the compressible laminar boundary-layer equations with given Mach number and wall temperature conditions (see White[24]). With these inflow conditions superimposed, viscous interaction at the leading edge of the plate can be neglected and the region (1) (see Fig. 1) is regarded as being identical to the free-stream condition.

At the outlet plane, a characteristic-based boundary condition is used in order to minimize any reflected waves. A no-slip wall condition with temperature equal to the adiabatic wall temperature at the inlet plane is applied at the lower boundary. At the upper surface of the computational domain, the free-stream quantities are applied in front of the oblique impinging shock wave, while downstream of the impinging shock location the upper boundary condition was given, initially, by applying the exact shock jump properties corresponding to a particular wedge angle. During the simulation, an integral formulation of a characteristic boundary condition is used at the upper surface. This formulation allows the specification of a reference condition, which is then superimposed with a time-accurate integration of all outgoing characteristics, computed using information within the computational domain. This allows the postshock conditions to be specified while also allowing outgoing waves to pass smoothly through the boundary without significant reflections.

C. Code validations

Sandham *et al.*[25] have demonstrated the capability of the above described numerical method for flows containing shock waves and some preliminary 2D results of the present oblique SBLI flow have been presented in Krishnan *et al.*[26] The code has been developed specifically to investigate transitional/turbulent boundary-layer phenomena by direct numerical simulation (DNS). For 2D simulations, the solution is advanced in time until there are negligible (less than 1%) changes in the flow properties of primary interest, such

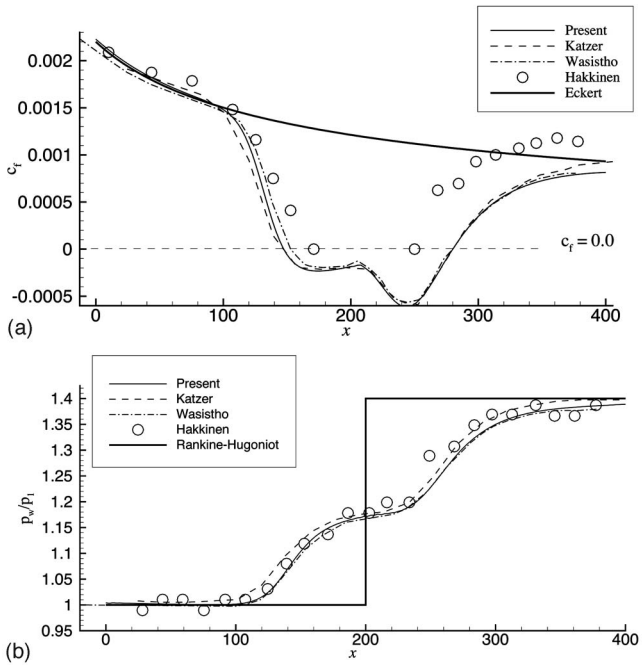

FIG. 2. Comparison of simulation results with experimental data and theory at $M_1=2.0$ and $Re^*_{\delta_1}=950$. (a) Distribution of the skin friction, c_f. (b) Distribution of the wall pressure, p_w/p_1.

as the separation bubble length and the skin friction coefficient. When the solution has converged the maximum residual amplitude is well below those of the forcing perturbation. For 3D simulations, disturbances are added to the wall boundary condition upstream of the separation location and the simulation is then continued in a time-accurate manner. Two validation tests were conducted, one for a steady 2D shock impingement at $M_1=2.0$ and the other for the growth of small-amplitude disturbances in a flat plate supersonic boundary layer at $M_1=1.6$ without the shock impingement.

The first test case considers the experimental flow conditions of Hakkinen *et al.*,[27] which were simulated numerically by Katzer[28] and Wasistho,[29] respectively, providing a 2D SBLI benchmark for the simulations presented in this paper. The simulations have supersonic inflow at $M_1=2.0$ and $Re_x=2.96\times10^5$ based on the distance from the boundary-layer origin to the shock impingement location in the absence of a boundary layer, which is equivalent to $Re_{\delta_1^*}=950$ based on the inflow boundary-layer displacement thickness δ_1^*. A baseline computational domain of 400×115 (based on δ_1^*) with a grid of 151×128 points is used, comparable to that adopted by Katzer[28] and Wasistho.[29] The overall shock pressure ratio is $p_3/p_1=1.4$, corresponding to a shock angle of $\beta_1=32.58°$ at $M_1=2.0$. Figure 2 gives a comparison of $c_f=2\tau_w/\rho_1U_1^2$, with $\tau_w=\mu_w(du/dy)_w$ and p_w/p_1 from the current simulation with previous computational and experimental results. A close agreement with previous investigations is obtained. The experiments give a shorter bubble and higher c_f, which may be due to three-dimensional effects in the experiment due to the presence of side walls, as discussed by Wasistho.[29] The second test case involves the computation of the growth of small-amplitude Tollmien-Schlichting waves in a flat plate supersonic boundary layer at

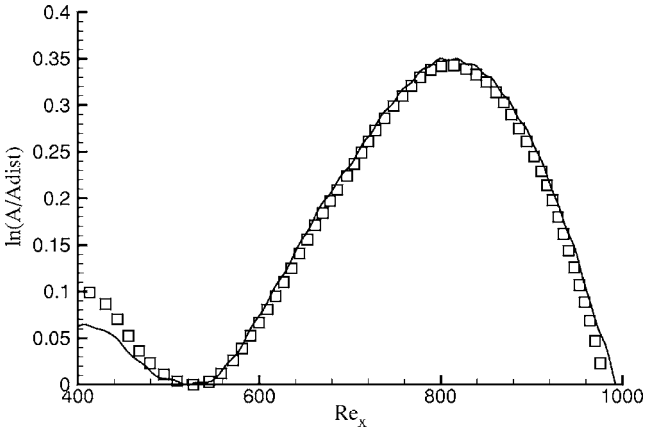

FIG. 3. Comparison of disturbance amplifications along the streamwise direction: Solid line: present simulation (DNS); symbol: Sandberg (Ref. 30) (linear Navier-Stokes solution).

$M_1=1.6$ and Reynolds number $Re_{\delta_1^*}=438.802$ based on the inflow boundary-layer displacement thickness. These conditions are identical to those considered by Sandberg.[30] A small-amplitude disturbance ($A_{dist}=0.0002$) was considered in the simulation. The growth of disturbance amplitude rate $[\ln(A/A_{dist})]$ and the distributions of the amplitude were obtained by a Fourier analysis of the flow variables over two disturbance periods. Figure 3 shows the growth and decay of the maximum amplitude of streamwise disturbances u' at various Re_x locations. The present results compare well with the linear Navier-Stokes solution of Sandberg.[30] Figure 4 gives the comparisons of the disturbance amplitude of three mode shapes ρ', u', T' at a location of $Re_x=700$ plotted against η, which is defined as $\eta=y\mathrm{Re}/\mathrm{Re}_x$, where $\mathrm{Re}=10^5$ is the free-stream Reynolds number; these also agreed well with linear Navier-Stokes solution. These two validations imply that the present code is capable of accurately computing both the 2D separated SBLI flow and the evolution of small-amplitude disturbances in supersonic boundary-layer flows.

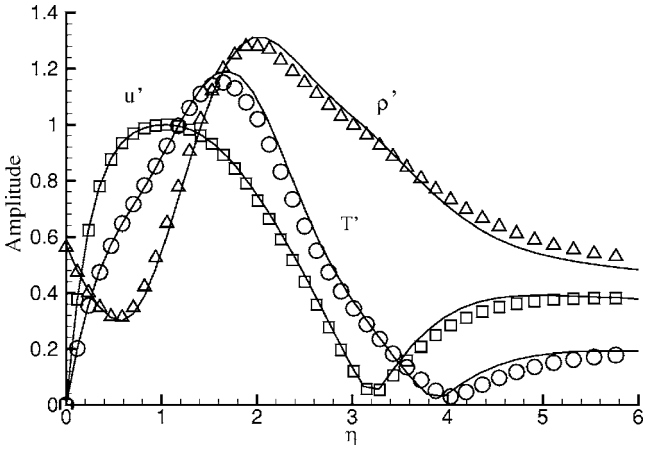

FIG. 4. Comparison of the disturbance amplitude of three mode shapes ρ', u', T' at a streamwise location of $Re_x=700$. Solid line: present simulation (DNS); symbol: Sandberg (Ref. 30) (linear Navier-Stokes solution).

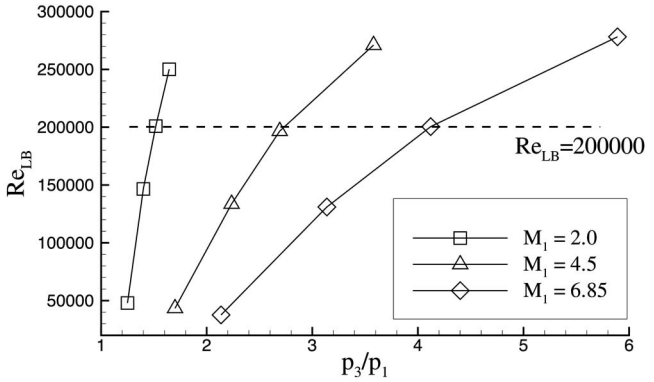

FIG. 5. Influence of Mach number M_1 and shock pressure ratio p_3/p_1 on the separation bubble length.

III. SELECTION OF PHYSICAL AND COMPUTATIONAL PARAMETERS

The intention of the present study is to compare the growth of small-amplitude disturbances in SBLI at different Mach numbers. As far as possible, we wish to remove the influence of other parameters, such as the Reynolds number and the length of the interaction region. To achieve this we consider a series of cases with a fixed interaction location Reynolds number. This Reynolds number is based on the distance from the origin of the boundary layer (i.e., the flat plate leading edge) to the point where the shock wave would impinge, in the absence of a boundary layer, denoted as Re_{xi}. Additionally, we impose a condition that the Reynolds number based on laminar bubble length is a constant (denoted as Re_{L_B}). This condition is set since it is known that the transition length Reynolds number in low-speed separation bubbles is approximately constant (Weibust *et al.*[31]). Any changes in disturbance growth factor can then be attributed to Mach number effects rather than difference in length of the separation zone. Additionally, we take the wall to be adiabatic for all cases to remove the influence of heat transfer to the wall surface.

It was shown in Krishnan *et al.*[26] that it is possible to collapse the results for 2D simulations with different bubble lengths using an extended scaling law $L_B=4.4P/(1+0.1P)$, where P is a pressure parameter defined as $P=(p_3-p_{\mathrm{inc}})/p_1$ and p_{inc} from Katzer[28] is the pressure in region (3) for incipient separation. Using this previous work as a guide, simulation parameters were chosen as $\mathrm{Re}_{xi}=3\times10^5$ and $\mathrm{Re}_{L_B}=2\times10^5$ for the three Mach numbers considered here.

Figure 5 shows the variation of Re_{L_B} with pressure ratio p_3/p_1. This can be used to set the pressure ratio at each Mach number to reach the chosen Re_{L_B}. Table I shows parameters for a series of 2D simulations designed to confirm that the numerical resolution is suitable. In each case, the computational box starts at $\mathrm{Re}_x=50\,000$ based on distance from the boundary-layer origin. For convenience, we use a simulation coordinate x measured from the inflow boundary, such that $\mathrm{Re}_x=U_1x/\nu_1+50\,000$. The reference length for the simulations is the inflow displacement thickness (δ_1^*). Computational box sizes are L_x and L_y in the streamwise and wall-normal directions, respectively, and the number of grid points in these directions are N_x and N_y, respectively.

Table II shows results from the simulations. The separation and reattachment points are denoted as x_s and x_r, respectively; the bubble height h_b is measured from the wall to the maximum height of the separation streamline. The final column shows that the bubble length Reynolds numbers are converged to within 1.1% of the target value of $\mathrm{Re}_{L_B}=2\times10^5$ for the fine grid cases 2, 4, and 6.

Figure 6 shows contours of density superimposed with streamlines and compares the interaction pattern for different Mach numbers. In each case, the incident oblique shock is reflected as an expansion fan and directs the flow towards the wall, leading to reattachment of the separating flow and the creation of a closed separation bubble. The separation bubble is found to be asymmetric, particularly at the higher Mach numbers ($M_1=4.5$ and $M_1=6.85$), and is displaced towards the upstream side. In addition, the bubble aspect ratio (ratio of bubble height to length) gets larger as the Mach number increases, although the bubble size itself is reducing.

IV. LOCAL LINEAR STABILITY ANALYSIS OF THE 2D BASE FLOWS

Small-amplitude disturbances in parallel compressible shear flows are governed by the compressible Orr-Sommerfeld equation, which assumes the form of disturbances as

$$\phi=\hat{\phi}(y)\exp[i(\alpha x+\beta z-\omega t)], \tag{9}$$

where $\phi=(\rho,u,v,w,T)^T$, α, and β are wavenumbers in the streamwise and spanwise directions, respectively, and ω is a frequency. The Orr-Sommerfeld system of equations may be written in a compact form as

TABLE I. Computational domain and grids for 2D simulations at given Mach number (M_1) and shock strength (p_3/p_1), corresponding to $\mathrm{Re}_{L_B}\approx2\times10^5$.

Case	M_1	$\mathrm{Re}_{\delta_1^*}$	$(L_x,L_y)/\delta_1^*$	(N_x,N_y)	β_1	p_3/p_1	T_w
1	2.0	732.63	(680, 30)	(385, 129)	33.075°	1.480	1.68
2	2.0	732.63	(680, 30)	(513, 193)	33.075°	1.480	1.68
3	4.5	1899.70	(260, 15.118)	(257, 129)	16.200°	2.667	4.40
4	4.5	1899.70	(260, 15.118)	(385, 193)	16.200°	2.667	4.40
5	6.85	3455.00	(150, 15.125)	(257, 129)	11.800°	4.121	8.83
6	6.85	3455.00	(150, 15.125)	(385, 193)	11.800°	4.121	8.83

TABLE II. Grid convergence study for 2D simulations illustrating the separation bubble length (x_s,x_r), the location of the bubble apex and the bubble length Reynolds number Re_{L_B}.

Case	M_1	x_{imp}	x_s	x_r	(h_b,x_b)	Re_{L_B}
1	2.0	341.24	192.94	460.44	(8.78, 326.64)	195 978
2	2.0	341.24	191.98	463.17	(8.70, 327.04)	198 681
3	4.5	131.76	64.97	168.72	(4.57, 115.73)	197 094
4	4.5	131.76	64.83	169.30	(4.60, 116.08)	198 462
5	6.85	72.40	33.31	91.38	(2.92, 59.58)	200 678
6	6.85	72.40	33.33	91.68	(2.95, 59.84)	202 268

$$\mathbf{L}\hat{\phi} = \omega \mathbf{K}\hat{\phi}, \tag{10}$$

where the matrix $\mathbf{L}$ depends on the base flow $(\bar{\rho},\bar{u},0,0,\bar{T})$, and the wavenumbers α and β. The matrix $\mathbf{K}$ only depends on the base flow. A temporal stability problem is defined by fixing α and β and finding ω from the eigenvalues of $\mathbf{K}^{-1}\mathbf{L}$. A spatial stability problem is defined by fixing ω and β and iterating on α until Eq. (10) is satisfied.

In compressible flows, the instability is classified as inflectional if a generalized inflection point

$$\frac{d}{dy}\left(\rho\frac{d\bar{u}}{dy}\right) = 0 \tag{11}$$

is present. For the shock impingement case at $M_1=2.0$, $M_1=4.5$, and $M_1=6.85$, Fig. 7 shows the variation of the y location of the generalized inflection point, denoted as y_i, normalized with the maximum value ($y_{i,\max}$, given in the figure caption) in the separation bubbles and plotted against Re_x. As previously noted, the location of the maximum bubble height (the apex of the bubble) moves forwards as M_1 increases, while the inflection point becomes closer to the wall. The latter is consistent with the reduction in bubble height indicated in Table II. Near the apex of the bubble, the inflection points follow an approximately linear variation with streamwise distance x, increasing over the front and decreasing over the rear of the bubble. Curvatures of these lines may be measured by a parameter C given by

$$C = \frac{U_R}{(d\bar{u}/dy)_i}\frac{d^2y_i}{dx^2}, \tag{12}$$

where U_R is a reference velocity, here taken as the inflow free-stream velocity. The parameter C is effectively the vorticity thickness of the shear layer divided by the radius of curvature of the $y_i(x)$ curve. Typical values range from $C\approx 0.004$ ahead of the bubble at $M_1=2.0$ to $C\approx 0.015$ at $M_1=6.85$. Curvatures at and after reattachment are smaller. Compared to the effect of curvature on mixing layers seen by Zhuang[32] (for example, a variation of 10% in growth rate for equivalent values of $C\approx 0.05$), the curvatures seen here appear to be small. Only at the apex of the bubble, where curvatures become $O(1)$, does the curvature appear to be significant. Note that the sign of the curvature is destabilizing near the separation point and near reattachment, but stabilizing at the apex of the bubble.

To show the linear stability characteristics, we consider a location halfway between the separation point and the apex of the bubble. Since the shear layer thickness varies relatively slowly with x, these locations are representative of the mean profiles found throughout the bubble region. Stability diagrams from viscous temporal stability analysis are shown in Figs. 8(a)–8(c) for the three Mach numbers, with contours of the imaginary part of the growth rate ω_i as a function of streamwise wavenumber α and spanwise wavenumber β. At $M_1=2.0$ there is a single peak, located near $(\alpha,\beta)=(0.13,0.18)$; i.e., the most unstable mode is an oblique first mode. At this peak, the phase speed is $c_{\mathrm{ph}}=\omega_r/\alpha=0.54$ and the wave angle is $\theta=\tanh^{-1}(\beta/\alpha)=53°$. A simple estimate of a density weighted convection velocity (Papamoschou and Roshko[33]) gives $U_c=\sqrt{T_w}/(1+\sqrt{T_w})=0.56$, in good agreement with the disturbance phase speed, while the simple formula of Sandham and Reynolds[34] for plane mixing layers ($M_c\cos\theta=0.6$) leads to a wave angle estimate of $\theta=46°$ [with $M_c=(U_e-U_c)/a_e=0.89$], a reasonable estimate of the angle of the most unstable mode.

At $M_1=4.5$ [Fig. 8(b)], the oblique first mode of instability has a peak at $(\alpha,\beta)=(0.14,0.37)$ (corresponding to a wave angle of $\theta=68°$). This mode still exists at $M_1=6.85$, peaking at $(\alpha,\beta)=(0.15,0.60)$ with a wave angle of $\theta=76°$. The simple estimations for oblique modes give $U_c=0.68$ (compared to $c_{\mathrm{ph}}=0.72$) at $M_1=4.5$ and $U_c=0.75$ (compared to $c_{\mathrm{ph}}=0.86$) at $M_1=6.85$. The wave angles are estimated as 65° at $M_1=4.5$ and 69° at $M_1=6.85$ [Fig. 8(c)]. These simple estimations thus remain useful for the oblique mode up to the highest Mach numbers studied.

At $M_1=4.5$ and $M_1=6.85$, the stability diagrams include additional Mack modes (second mode, third mode, etc.) of instability. Previous examples for shock-induced separation bubbles were shown in Pagella *et al.*[9,16] at $M_1=4.8$; the present results are consistent with those findings. At $M_1=4.5$ the most unstable mode is the second mode, with a growth rate of $\omega_i=0.026$ at $(\alpha,\beta)=(0.41,0.0)$ and a phase speed of $c_{\mathrm{ph}}=0.82$. The Mack modes are most unstable in 2D and propagate with supersonic speed relative to the wall. A weaker third mode can be seen towards the right of the plot at $(\alpha,\beta)=(0.97,0.0)$. At $M_1=6.85$ [see Fig. 8(c)], the second

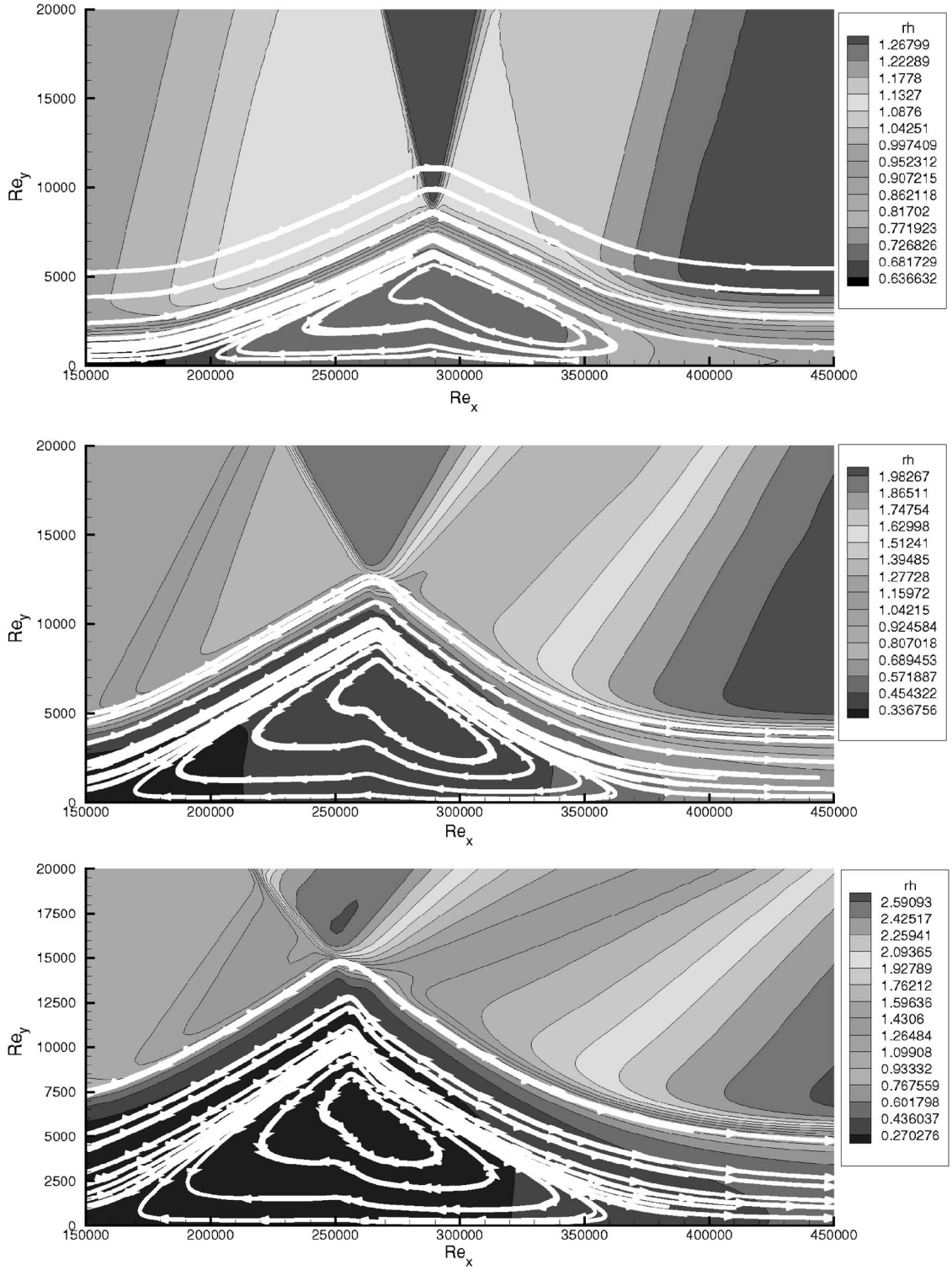

FIG. 6. Density contours show the separation bubble length, shape and location with superimposed streamlines for different Mach numbers: $M_1=2.0$ (top); $M_1=4.5$ (middle); $M_1=6.85$ (bottom).

and third modes have comparable maximum growth rates. A much weaker fourth mode can be seen at the right-hand edge of the plot. In contrast to the oblique modes, the locations of the most unstable Mack modes vary along the length of the bubble. This is due to the basic physical mechanism of the Mack mode instability, which involves a resonance of acoustic waves located between the critical layer and the wall. Anticipating that the local height of the bubble will be an important parameter, we plot αy_i against Re_x in Fig. 9 for the most unstable Mack modes (the second mode at $M_1=4.5$ and the second and third modes at $M_1=6.85$). The variation of αy_i along the bubble is only of the order ±10%, whereas y_i varies by a factor of roughly three (Fig. 7). This means that particular Mack modes are only unstable over short distances

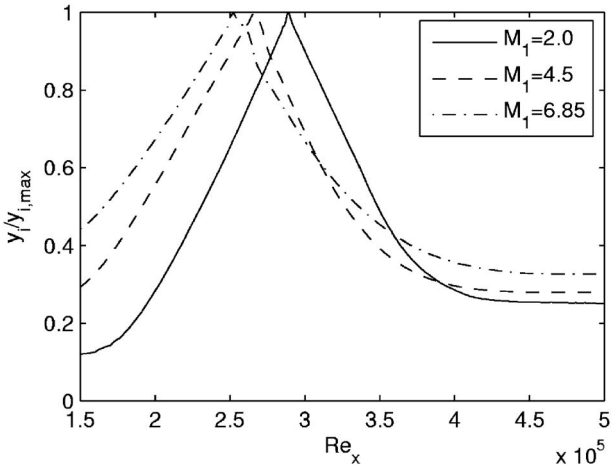

FIG. 7. Streamwise variation of the location of the generalized inflection point, plotted as $y_i/y_{i,\max}$ (where $y_{i,\max}=10.59$, 6.34, and 4.25 for $M_1=2.0$, 4.5, and 6.85, respectively) in the separation bubbles.

along the bubble length, with reduced overall growth rates. This will be further quantified in Sec. VI.

V. SIMULATION OF 3D FLOWS WITH SMALL AMPLITUDE DISTURBANCES

The linear stability results of the previous section were used as a guide to fix the spanwise box size L_z such that the most unstable modes are contained within the computational domain. The dimensions L_x and L_y are the same as in the 2D simulations detailed in Table I. The laminar base flow is perturbed by injecting low momentum fluid with zero net mass flow through the plate surface for which a vertical velocity is specified as $v_{\text{inj}}(x,t)=A\Omega$, where A is the amplitude and Ω is a random number (uniformly distributed on $[-0.5,0.5]$ and independently generated at each x, z, and t within the forcing strip) giving white-noise forcing in space (x and z) and time (t). The injection starts at x_{st} and ends at x_{en} and spans the whole width of the computational domain. Table III shows computational parameters for two values of A for each Mach number (cases 7–12).

The amplitude A has been chosen such that the response of boundary layer is still within the linear growth region. Figure 10 shows root-mean-square (RMS) values for the three velocity components for the two different amplitudes of white-noise forcing given in Table III. In each case, the RMS values (fluctuations are computed relative to the local spanwise-averaged values to remove the influence of small changes in the base flow) have been divided by A to scale the amplitude out of the problem. Note that the amplitude of the forcing perturbation for $M_1=4.5$ and $M_1=6.85$ is an order of magnitude larger than that for $M_1=2$, but collapse of the lines (low A) with the symbols (high A) demonstrates the linearity of results. The curves have a peak near the forcing location of $\text{Re}_x\approx 100\,000$. Downstream these disturbances grow up to the apex of the bubble. For the two higher Mach numbers in particular, there is a sharp drop in the RMS streamwise velocity at the apex of the bubble [$\text{Re}_x\approx(2.6-2.8)\times 10^5$]. This is followed by renewed growth over the rear portion of the bubble and reduced growth rates after

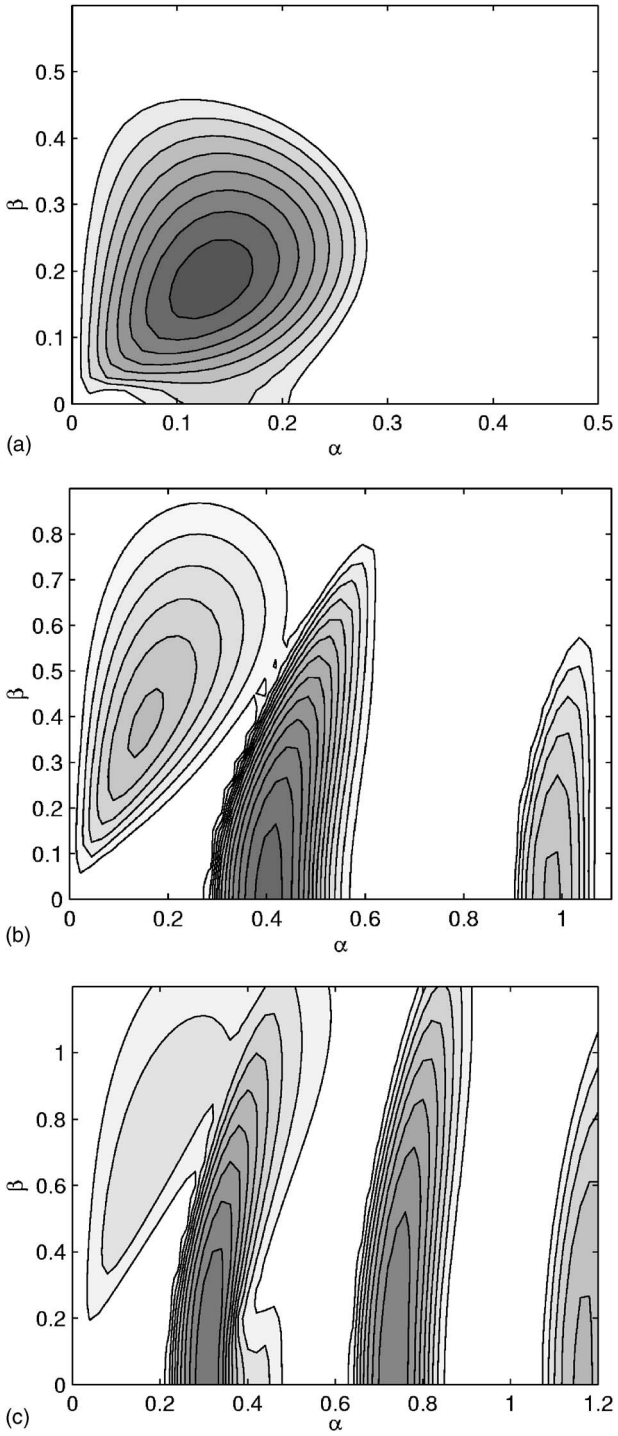

FIG. 8. Contours of temporal growth rate ω_i at (a) $M_1=2.0$, (b) $M_1=4.5$, and (c) $M_1=6.85$. Contours start from 0.002 and continue upwards with steps of 0.002 in all cases. The dark color corresponds to higher values.

the reattachment. Drops in disturbance energy at the shock impingement location have also been seen in Teramoto.[18]

Several other important points can be made in the context of Fig. 10. First, we note that all cases gave time-invariant statistics; i.e., the flow is demonstrated to be convectively unstable. This is important because the bubbles contain significant amounts of reverse flow and it is believed that bubbles with higher pressure ratio (e.g., for $M_1=2.0$ and $p_3/p_1=1.91$; see Teramoto[18]) can sustain transition to turbu-

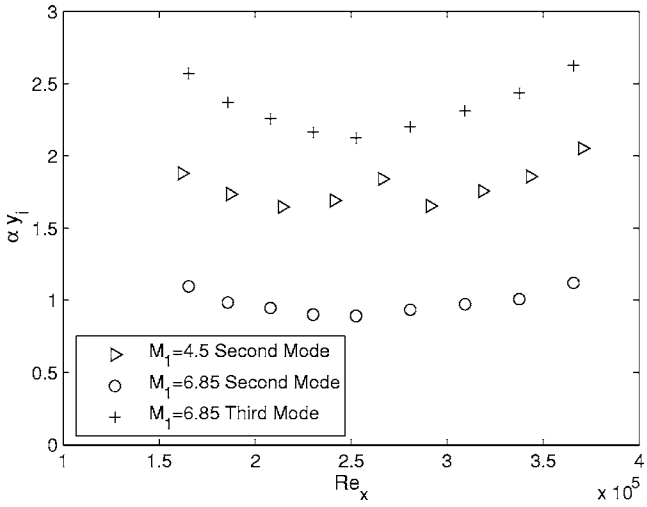

FIG. 9. Streamwise variation of the quantity αy_i for the most important Mack modes (second and third modes) at $M_1=4.5$ and $M_1=6.85$.

lence without appearance of upstream turbulence. Second, we note that the growth curves for different velocity components show different streamwise variations. This indicates that there are significant nonparallel effects present and that the locally parallel flow assumption of the LSA described in the previous section may not be justified.

Figure 11 shows isosurfaces of vertical vorticity ω_y, which effectively illustrates the 3D flow structures. The $M_1=2.0$ results appear to be in good agreement with the most unstable modes from the previous linear stability analysis. The dominant spanwise mode corresponds to $\beta=0.196$, which compares reasonably well with the most unstable oblique mode from the LSA, which was $\beta=0.18$ [Fig. 8(a)]. Both the $M_1=4.5$ and $M_1=6.85$ cases [Figs. 8(b) and 8(c)] show predominately streamwise structures. Such streamwise structures, for example on compression ramp experiments (see Simeonides and Haase[37]), are often attributed to a Görtler mechanism based on streamwise curvature. However, we do not observe a strong correlation between the disturbance growth rate and the streamwise curvature given by Eq. (12).

Figure 12 gives the RMS values of kinetic energy in terms of an n-factor defined as $n=\ln[e(x)/e(x_s)]$ with $e(x)=\max\left[\sqrt{\frac{1}{2}\overline{u_i'u_i'}(x)}\right]$ and $u_i'=u_i-\langle u_i\rangle$, where $\langle u_i\rangle$ denotes the spanwise averaging. The values at $\mathrm{Re}_{x_s}=1.5\times10^5$ are taken as reference data. At $M_1=2.0$ the n-factor increases up to values 6–7 during the separation and after the reattachment. By contrast, at $M_1=4.5$ and $M_1=6.85$, the growth of the n-factor is relatively small and finally reaches a value around 2.

The preceding simulations have demonstrated that unstable modes emerge naturally from the white-noise forcing, with characteristic flow structures for all Mach numbers. For comparison with linear stability theory, it is helpful to run additional calculations with fixed frequency and spanwise wavenumber combinations, where a vertical wall velocity is specified as $v_{inj}(z,t)=A\sin(\omega t)\cos(\beta z)$ over the disturbance strip. These forcing parameters were determined with reference to the earlier white-noise simulations and associated stability calculations, which are reported in the next section. Four additional simulations (cases 13–16 in Table III) are considered. In each case only one spanwise wavelength is used (in addition, the amplitude is reduced to $\sim10^{-6}$ for $M_1=2.0$ simulations to retain linear growth of the disturbances). Two simulations use the same grid resolution as those of cases 7–12, while the remaining two include 50% more grid points in all three directions so that any grid dependency of the results can be addressed.

Figure 13 gives a comparison of the RMS kinetic energy variations along the streamwise direction for these simulations. Qualitatively, the results are similar to the earlier simulations, indicating that the most unstable modes can emerge rapidly from white-noise forcing. The grid refinement study shows that sufficient grid points have been used. In particular, it should be noted that the large drop in disturbance amplitude at the location where the shock impinges on the top of the separation bubble at $M_1=4.5$ is not sensitive to the grid. Figure 14 shows isosurfaces of vertical vorticity ω_y, illustrating the 3D flow structures. The oblique mode with $(\omega,\beta)=(0.056,0.196)$ simulated at $M_1=2.0$ produces a criss-cross pattern, consistent with the superposition of two equal and opposite oblique instability waves. At $M_1=4.5$, oblique mode forcing with $(\omega,\beta)=(0.014,0.95)$ shows predominately longitudinal streamwise structures, as seen in the white-noise-forced cases. This confirms that traveling insta-

TABLE III. Computational domain and grids for 3D simulations with small-amplitude disturbances of white-noise forcing (cases 7–12) and oblique mode forcing (cases 13–16).

Case	M_1	$(L_x,L_y,L_z)/\delta_1^*$	(N_x,N_y,N_z)	A	(x_{st},x_{en})
7	2.0	(680, 30, 64)	(513, 129, 65)	0.001	(51.86, 59.64)
8	2.0	(680, 30, 64)	(513, 129, 65)	0.002	(51.86, 59.64)
9	4.5	(260, 15.118, 32)	(257, 129, 65)	0.01	(20, 23)
10	4.5	(260, 15.118, 32)	(257, 129, 65)	0.02	(20, 23)
11	6.85	(150, 15.125, 32)	(257, 129, 65)	0.01	(11, 12.65)
12	6.85	(150, 15.125, 32)	(257, 129, 65)	0.02	(11, 12.65)
13	2.0	(680, 30, 32)	(513, 129, 33)	0.000 001	(51.86, 59.64)
14	2.0	(680, 30, 32)	(769, 193, 49)	0.000 001	(51.86, 59.64)
15	4.5	(260, 15.118, 6.6)	(257, 129, 13)	0.001	(20, 23)
16	4.5	(260, 15.118, 6.6)	(385, 193, 19)	0.001	(20, 23)

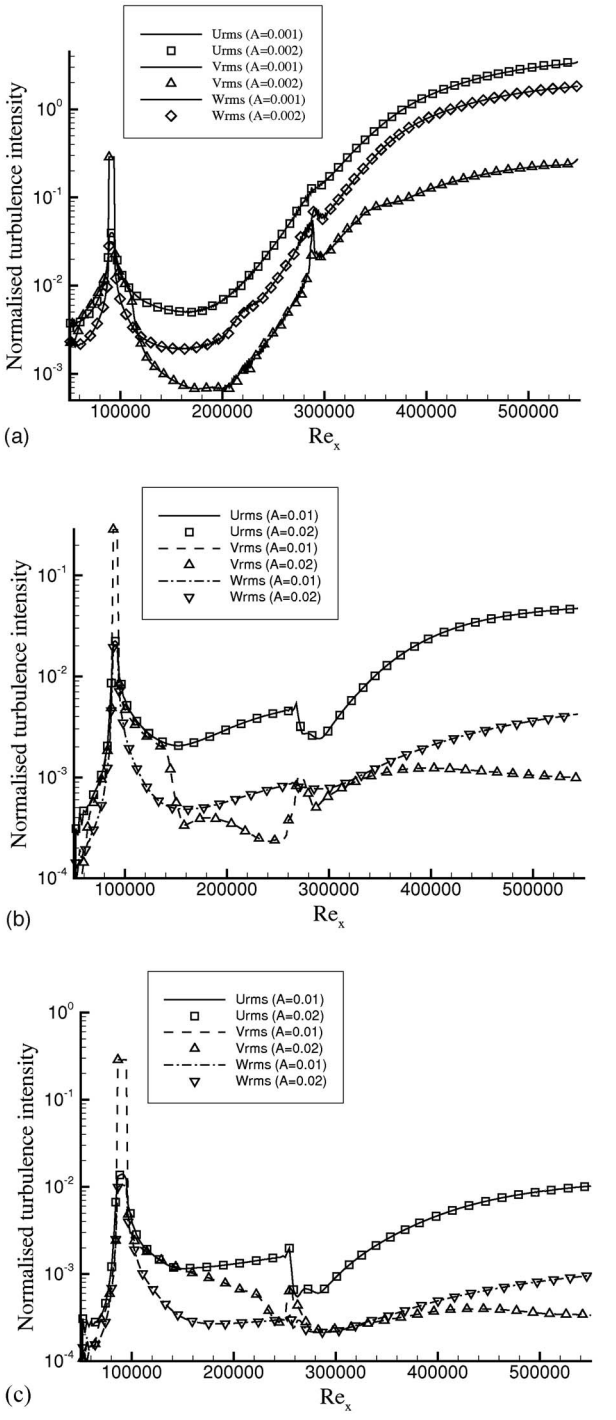

FIG. 10. Normalized turbulence intensity from simulations with two different amplitudes of white-noise disturbances, showing the linear growth of the disturbances. (a) $M_1=2.0$; (b) $M_1=4.5$; (c) $M_1=6.85$.

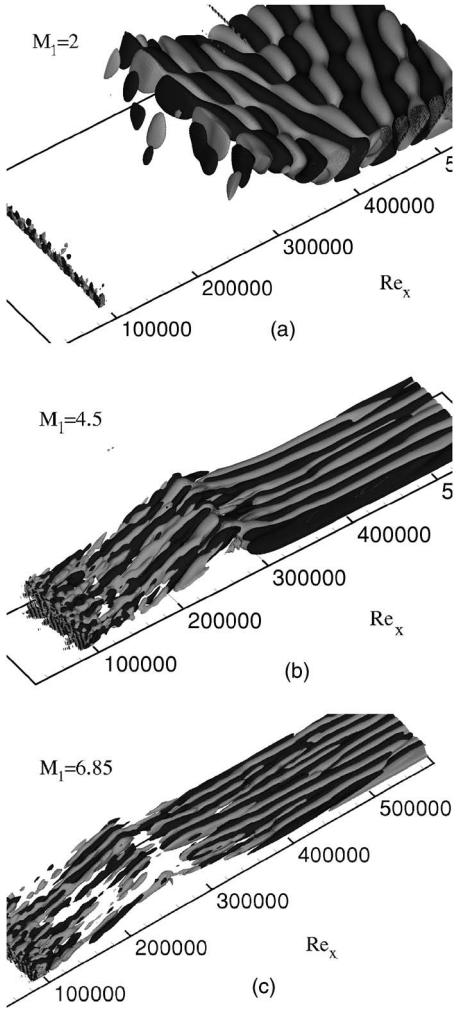

FIG. 11. Isosurfaces of vertical vorticity ω_y show the near-wall streamwise structures at three Mach numbers ($M_1=2.0$, 4.5, and 6.85). Dark color: $\omega_y=-10^{-5}$; light color: $\omega_y=+10^{-5}$.

bility waves at low frequency are capable of producing the streamwise structures seen in the earlier white-noise forcing simulation.

VI. GROWTH (*n*-FACTOR) PREDICTIONS AND DISCUSSION OF NONPARALLEL EFFECTS

Linear stability predictions of disturbance growth are obtained via the *n*-factor calculated as

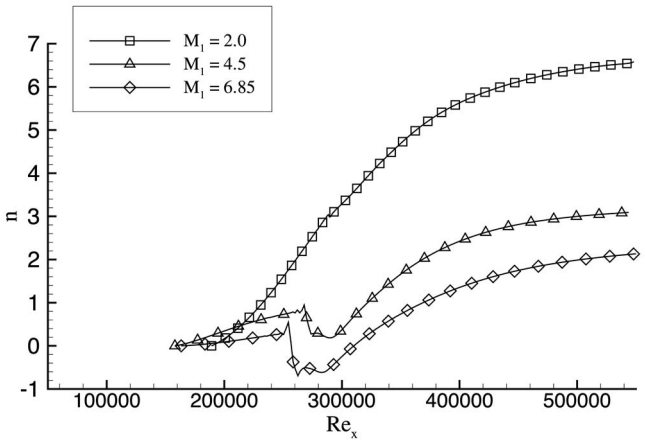

FIG. 12. Simulated growth *n*-factors measured by the RMS kinetic energy for three Mach numbers from small amplitude disturbances of white-noise forcing.

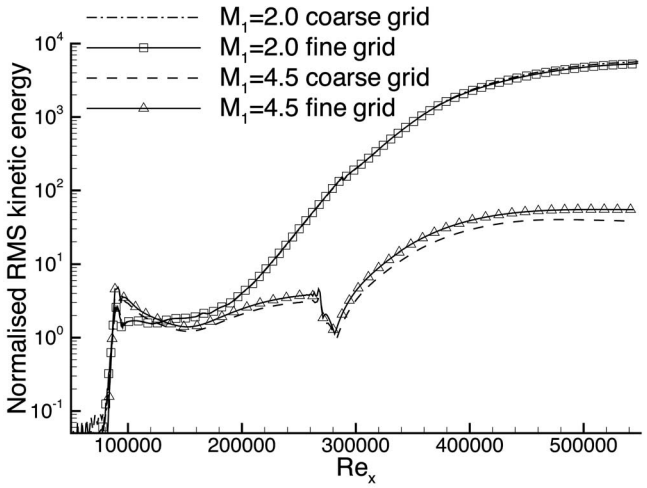

FIG. 13. Simulated RMS kinetic energy (normalized with amplitude) for $M_1=2.0$ and $M_1=4.5$ from small-amplitude disturbances of oblique mode forcing.

$$n = -\int_{x_s}^{x} \alpha_i dx, \tag{13}$$

where x_s is the separation location, preferred here to the lower branch, to allow comparisons with the simulations of the previous section. Spatial stability theory is carried out to determine α for combinations of (ω,β). The combinations that lead to the greatest n are deemed the most dangerous disturbances.

Figure 15 shows n-factor predictions based on stability theory. For consistency with the earlier DNS results, we have limited the possible values of β to those that are supported on the periodic computational domains employed in the previous section. At $M_1=2.0$, $(\omega,\beta)=(0.056,0.196)$ gives the highest overall n-factor for inviscid stability theory. The effect of viscosity is shown by the second curve plotted for $M_1=2.0$ on Fig. 15, with growth rates and n-factors reduced by around 10%. Even with the viscous effects, the overall growth rates are still above the linear Navier-Stokes computations of the previous section (cf. Fig. 12); quantitative comparisons will be made after we have considered nonparallel effects. Figure 15 also shows the growth rates for the most unstable oblique modes at $M_1=4.5$ and $M_1=6.85$. The most dangerous modes are oblique modes $(\alpha,\beta)=(0.245,0.58)$ at $M_1=4.5$ and $(\alpha,\beta)=(0.127,0.48)$ at $M_1=6.85$, respectively. Overall growth rates lead to n-factors of less than 2, and are even lower when viscous effects are included.

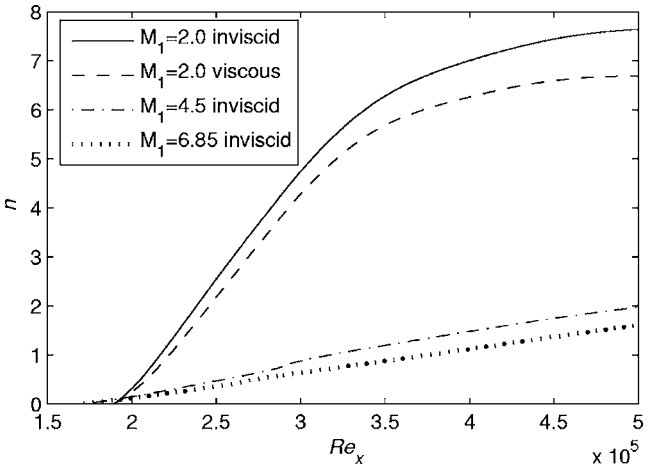

FIG. 15. Growth n-factors illustrating the effects of Mach number and viscosity.

The amplification of the second mode is strongly dependent on frequency and the most unstable frequency varies as the local bubble height varies. This leads to low overall growth factors of the second mode along separation bubbles,

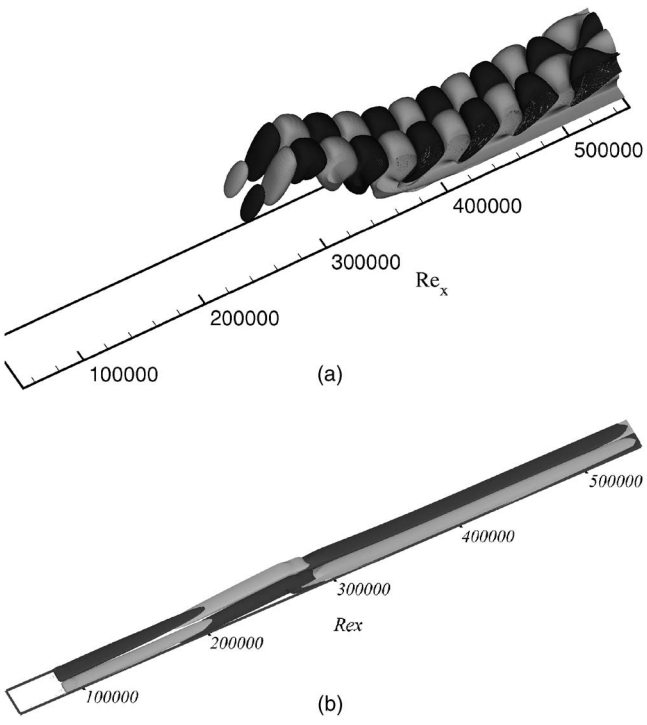

FIG. 14. Isosurfaces of vertical vorticity ω_y show the near-wall streamwise structures from oblique-mode forcing DNS: $\omega_y=\pm 10^{-5}$ for $M_1=2.0$ and $\omega_y=\pm 10^{-3}$ for $M_1=4.5$; dark color for negative value and light color for positive value.

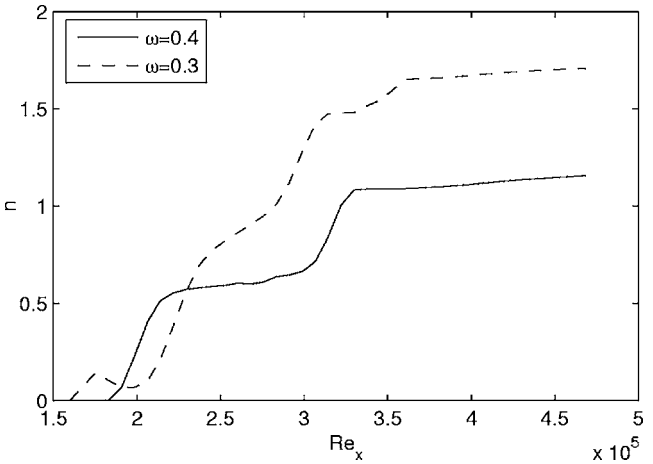

FIG. 16. Growth n-factors for the Mack modes ($\beta=0.0$) of different frequencies at $M_1=4.5$. Note the low overall growth factors, despite the high localized growth rates.

as was seen in the study of compression corner flow by Balakumar *et al.*[9] Figure 16 shows the growth of the n-factors for the second mode at frequencies $\omega=0.3$ and $\omega=0.4$ for $M_1=4.5$. The high frequency case is most unstable at locations approximately halfway between the separation point ($Re_x \approx 2.0\times 10^5$) and the bubble apex and halfway between the bubble apex and reattachment ($Re_x \approx 3.3\times 10^5$). The n-factor plot shows high growth rates in these regions, with a plateau where this particular frequency is close to neutral; i.e., near the apex of the bubble. The lower frequency case shows most growth towards the center of the bubble. In both cases the overall growth n-factors are very small (corresponding to only a factor of 10 growth in amplitude) even though the second modes are locally the most unstable modes.

Nonparallel effects are important in the current problem and simulations have therefore been made using the parabolized stability equations (see Herbert,[10] Hein *et al.*[11]). The equation set in this case is given by

$$\mathbf{M}\frac{d\hat{\phi}}{dx} = (\omega\mathbf{K} - \mathbf{L} - \mathbf{L}')\hat{\phi}. \tag{14}$$

The **L** and **K** matrices are the same as in Eq. (10). The matrix **M** multiplies streamwise derivatives of the stability variables $\hat{\phi}$, while $\mathbf{L}'$ contains nonparallel terms. The system is derived by neglecting terms of order Re^{-2} and assuming that $\bar{v}$ is $O(Re^{-1})$. The latter assumption is not strictly satisfied here since v fluctuations (v') are about a tenth of the free-stream velocity, but the inclusion of higher order nonparallel terms did not significantly change the results. A starting distribution for $\hat{\phi}$ at some prescribed x is given from parallel flow stability theory and the solution is then marched downstream. At each step the wavenumber is adjusted to maintain the norm

$$\int \hat{u}_i^{\dagger}\frac{\partial \hat{u}_i}{\partial x} = 0, \tag{15}$$

where "†" denotes a complex conjugate. Growth factors are computed using integrated kinetic energy, including the growth contained in α as well as the growth contained in $\hat{u}_i$. In the current applications, the smallest stable streamwise step size is taken to minimize truncation errors. Improved results were obtained when we neglected the streamwise pressure gradient, as suggested in Herbert.[10] However, the PSE calculations discussed here remain sensitive to the numerical scheme; this is believed to be because the separation bubbles are close to the boundary of absolute instability, where the PSE becomes invalid. These effects will become more severe with increasing Mach number, thus we consider the effectiveness of the PSE only at the two lower Mach numbers $M_1=2.0$ and $M_1=4.5$.

Figure 17 compares the results of the DNS with the PSE at $M_1=2.0$. Note that the disturbance growth predicted by the DNS with harmonic forcing is slightly larger than that predicted with white-noise forcing (Fig. 12), as expected. It can be seen that the PSE accounts for the spatial development of the base flow but leads to reduced growth rates compared to the DNS. The discrepancy may be due to the fact that truncation errors can be significant in PSE, but step sizes cannot

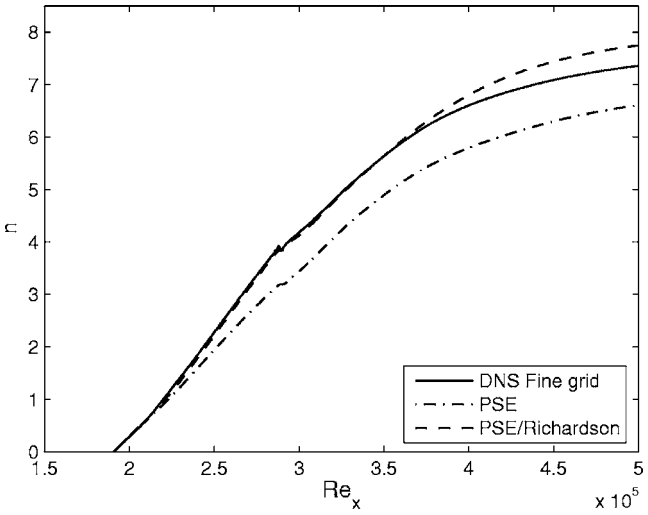

FIG. 17. Growth n-factors for the most amplified oblique first-mode disturbances at $M_1=2.0$ ($\omega=0.056$, $\beta=0.196$), comparing DNS with PSE.

be reduced due to stability considerations. To provide a better estimate we apply a Richardson extrapolation to PSE results obtained on two different grids (with sizes two and four times the DNS grid spacing), bringing an improved PSE estimate (shown with the dashed line on the graph) into much closer agreement with the Navier-Stokes solution. It is important to note that the PSE approach is capable of predicting the small dip in growth of the n-factor at $Re_x=2.85\times 10^5$, which results from the reduction in the streamwise RMS at that location (see Fig. 10).

The reduction of disturbance energy close to the shock impingement at the apex of the bubble becomes much more pronounced at the higher Mach numbers. The linear e^n method (Fig. 15) was incapable of predicting this. The PSE at $M_1=4.5$ for the most unstable frequencies of linear theory led to damped disturbances, indicating a very strong effect of the nonparallel terms. The parameters were varied until a maximum overall growth rate was obtained for $\omega=0.014$ and $\beta=0.95$. A comparison of the resulting PSE prediction with

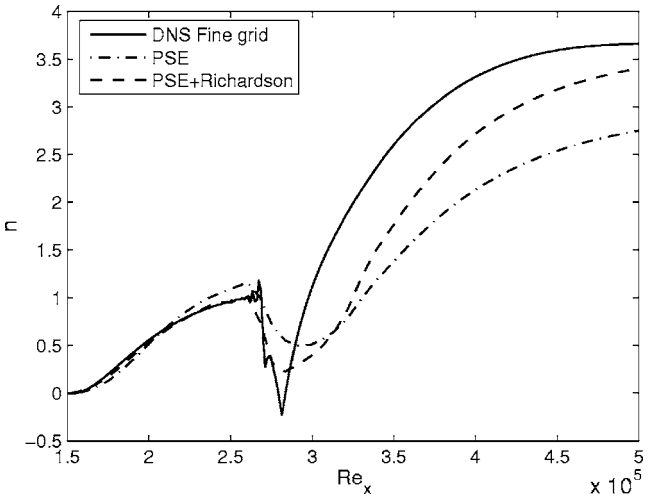

FIG. 18. Growth n-factors for the most amplified oblique first mode disturbances at $M_1=4.5$ ($\omega=0.014$, $\beta=0.95$), comparing DNS with PSE.

the DNS is shown in Fig. 18, also including the results of a Richardson extrapolation applied in the same way as at $M_1=2.0$. Again, the *n*-factors predicted by the DNS with harmonic forcing are slightly larger than those predicted with white-noise forcing (Fig. 12). Agreement between the PSE and DNS curves is good over the front half of the bubble and the PSE is capable of predicting the dip in disturbance amplitude at the bubble apex. However, the method underpredicts the growth rates during the recovery region after the shock impingement; this is probably caused by the relatively large step sizes that had to be adopted for stability reasons. Qualitatively, the PSE is successful and the spanwise wavenumber for the oblique mode with the highest growth rate is $\beta=0.95$ (corresponding to a wavelength of 6.6), which matches well with the DNS results [Fig. 11(b) exhibits spanwise wavelengths of the order of 5–8]. In addition, the frequency from the PSE prediction ($\omega=0.014$) is low, which is in qualitative agreement with the long quasi-streamwise structures seen in the white-noise-forced DNS.

VII. EARLY STAGE OF NONLINEAR BREAKDOWN TO TURBULENCE

In the previous sections, we studied the linear growth of small-amplitude disturbances by using DNS, LST, and PSE. Some previous investigations (e.g., Rai and Moin,[35] Pirozzoli *et al.*,[36] Teramoto[18]) suggested that at low Mach number ($M_1=2.0$) the shock-wave/boundary-layer interaction will undergo an oblique breakdown and finally transition to turbulence. As this study confirms that the two high Mach numbers $M_1=4.5$ and $M_1=6.85$ have very similar linear growth rate, the final breakdown process is likely to be similar. Hence, in this section we focus on the discussion of the early stage of nonlinear breakdown of disturbances and transition to turbulence in the Mach 4.5 flow.

Comparing to the 3D simulation case 10 described in Sec. V, the present three-dimensional simulation uses a computational box with the same dimensions in the streamwise and the wall normal directions, but a smaller spanwise width equal to $8\delta_1^*$. This width should be sufficiently wide for one wavelength of the dominant response [as seen in Fig. 11(b)]. A grid of $257\times129\times17$ ($N_x\times N_y\times N_z$) was chosen with a corresponding $(\Delta x^+,\Delta y_1^+,\Delta z^+)=(22.0,1.0,11.0)$, respectively, close to a fully resolved DNS. The most unstable frequencies and the wavenumbers obtained from the LST/PSE analysis are used to force the nonlinear breakdown and transition in the flow. These disturbances are introduced upstream of the separation bubble by a localized blowing/suction strip at the wall surface via the wall-normal velocity disturbance (v') as

$$v' = A\exp[-0.125(x-25.0)^2]\sin(\omega t)\cos(\beta z) + 2\%\ \text{random noise}, \tag{16}$$

where A is the amplitude, β is the spanwise wavenumber, and ω is the frequency of the disturbance. For the oblique mode disturbance, $\omega=0.014$ and $\beta=0.95$ were used (since they are the most unstable disturbances at this Mach number). In the case of the second-mode disturbance, $\omega=0.3$ and $\beta=0$ were taken.

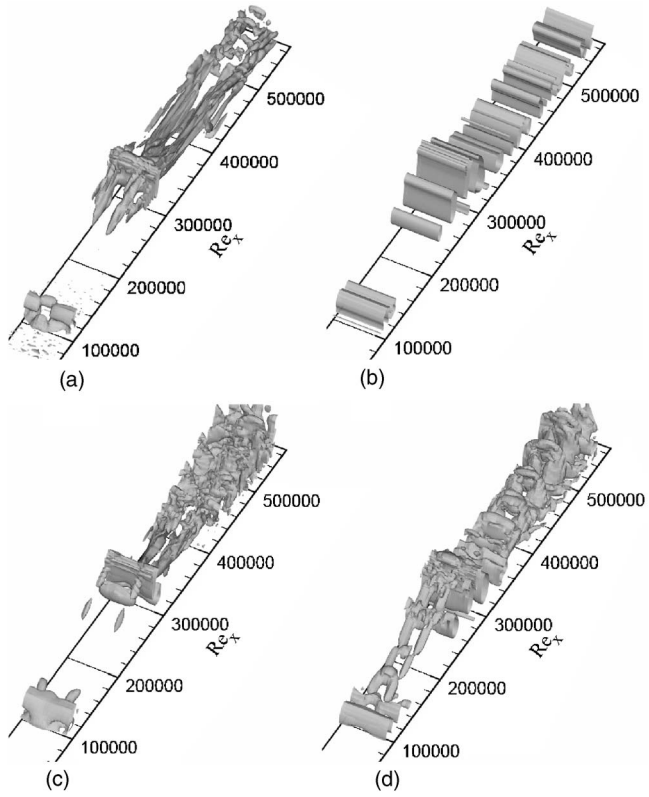

FIG. 19. Isosurfaces of second invariant of the velocity gradient tensor ($\Pi=-0.0006$) showing the coherent structures in the flow. (a) Oblique first mode with $A=0.1$, (b) second mode with $A=0.1$, (c) oblique first mode with $A=0.1$+second mode with $A=0.02$, and (d) oblique first mode with $A=0.1$+second mode with $A=0.1$.

Figure 19(a) plots the isosurfaces of second invariant [$\Pi=(\partial u_i/\partial x_j)(\partial u_j/\partial x_i)$] at a value of −0.0006, showing the evolution of an oblique first-mode disturbance ($A=0.1$, $\omega=0.014$, $\beta=0.95$) over the separation bubble and after the reattachment. In comparison to the simulation with small-amplitude white-noise disturbances [see Fig. 11(b)], the finite-amplitude oblique disturbance triggers stronger stationary streamwise structures by the oblique mode interaction. An enhanced lift-up of the near-wall fluid in between these streamwise structures induces strong shear layers away from the wall. The roll-up of these shear layers further produces spanwise structures in the flow, which can be identified from Fig. 19(a) near the outflow boundary. Simulation with $A=0.1$ of the second-mode disturbance ($\omega=0.3$, $\beta=0.0$) by itself shows spanwise structures in the flow but no sign of transition onset [see Fig. 19(b)]. Very weak streamwise vortices were observed in this flow due to the small-amplitude random disturbances (as in case 10 described in Sec. V). These nonlinear calculations confirm the smaller growth rates of the second-mode disturbances with *n*-factors between 2 and 3.

A combination of a finite-amplitude ($A=0.1$) oblique-mode disturbance ($\omega=0.014$, $\beta=0.95$) with a small-amplitude ($A=0.02$) second-mode disturbance ($\omega=0.3$, $\beta=0.0$) is found to be effective in advancing the transition onset. Figure 19(c) shows that the streamwise structures experience an earlier breakdown for $\mathrm{Re}_x \geqslant 400\,000$, compared

to $Re_x \geq 500\,000$ for the oblique-mode-alone disturbance [see Fig. 19(a)]. A final simulation was performed with equal ($A=0.1$) amplitudes of the oblique first mode and the second mode. Immediately downstream of the disturbance strip, a hairpin vortex structure was generated, which develops smaller structures upstream of the shock impingement location. However, towards the reattachment and beyond this location the breakdown ceases and there is a re-emergence of the second mode, with spanwise-coherent structures [see Fig. 19(d)]. The final breakdown in this case occurs via a breakdown of hairpin-shaped structures for $Re_x \geq 450\,000$.

Simulations at $M_1=6.85$ have also been carried out using 10% oblique mode ($\omega=0.014$, $\beta=0.62$) disturbance, 2% second-mode ($\omega=0.4$, $\beta=0.0$) disturbance, and 2% random noise. Results show energetic streamwise structures; however, there is no breakdown to turbulence within the present computational domain ($Re_x \approx 5.5\times 10^5$ at the exit).

VIII. CONCLUSIONS

The two-dimensional Navier-Stokes simulations of an oblique shock wave impinging on a flat plate laminar boundary layer were carried out at three Mach numbers of $M_1=2.0$, $M_1=4.5$, and $M_1=6.85$. The results illustrated the expected features for this type of shock-wave/boundary-layer interaction; namely, the separation and subsequent reattachment of the boundary layer, and the consequent formation of additional compression and shock waves. Comparisons of surface pressure and skin friction distributions with those of previous numerical simulations by other workers at $M_1=2.0$ show almost identical results.

A parametric study of the effect of the impinging shock strength was carried out at the Mach numbers described above in order to set up baseline flow conditions for subsequent three-dimensional simulations in which the linear growth of artificially introduced small-amplitude disturbances was explored. The instabilities were initially seeded with white noise so as to include many frequency and spanwise wavenumber combinations. At $M_1=2.0$, the emergent structures have frequencies and wavenumbers close to those predicted from parallel flow linear stability theory. Further simulations were carried out for fixed frequency and spanwise wavenumber and the PSE approach was demonstrated to give a close match to the disturbance envelope from the Navier-Stokes calculations.

At $M_1=4.5$ and $M_1=6.85$, the picture was very different. The parallel flow linear stability theory could not predict the large reductions in disturbance kinetic energy near the apex of the bubble. The inclusion of nonparallel effects in the PSE, together with the disturbance-evolution formulation was capable of predicting quantitatively the disturbance growth over the front of the bubble and qualitatively captured the extinction process at the apex of the bubble, where the shear-layer curvature is convex (stabilizing) and very large. Downstream of the bubble apex, there is a poor correlation between shear layer curvature and disturbance instability. Thus, although nonparallel effects are extremely important, it seems that for these flows they should not be parametrized with a single curvature parameter (in contrast to the Görtler problem). The structures that form at the higher Mach numbers are predominantly streamwise in nature, with spanwise wavenumbers in close agreement with the most amplified modes from the PSE. By contrast, the parallel flow linear stability predictions lead to erroneous estimates of the most unstable frequency and spanwise wavenumber and are unable to predict the reductions of disturbance kinetic energy at the apex of the bubble.

Overall the observations suggest that parallel flow stability results are of only limited use for high Mach number shock/boundary-layer interactions. The PSE approach was capable of producing useful estimations for these flows, but for any higher interaction strengths the basic instability mechanism is known to change from convective to absolute in nature, violating the assumptions of the PSE.

Finally, 3D Navier-Stokes simulations using finite-amplitude disturbances show that the strength of the streamwise structures produced by the oblique-mode disturbances dominates the early-stage of final breakdown process in the shock-wave/boundary-layer interaction at Mach 4.5. The additional unstable second-mode disturbances are found to enhance the nonlinear breakdown of laminar transition to turbulence. This breakdown has not been observed when the same disturbances were introduced for a Mach 6.85 flow, indicating that it is relatively more resistant to transition.

ACKNOWLEDGMENTS

The first author would like to thank the support from Kingston University under the "Promising Researcher Fellowship Scheme" during the course of the study. The authors also would like to acknowledge the parallel computing time support from the University of Southampton and the UK Turbulence Consortium sponsored by the Engineering and Physical Science Research Council, UK.

[1] T. Adamson, Jr. and A. Messiter, "Analysis of two-dimensional interactions between shock waves and boundary layers," Annu. Rev. Fluid Mech. **12**, 103 (1980).
[2] J. Delery, "Shock phenomena in high speed aerodynamics: still a source of major concern," Aeronaut. J. **1**, 19 (1999).
[3] D. Dolling, "Fifty years of shock-wave/boundary-layer interaction research: what next?" AIAA J. **39**, 1517 (2001).
[4] D. Knight, H. Yan, A. G. Panaras, and A. Zheltovodov, "Advances in CFD prediction of shock wave turbulent boundary layer interactions," Prog. Aerosp. Sci. **39**, 121 (2003).
[5] W. S. Saric, H. L. Reed, and E. B. White, "Stability and transition of three-dimensional boundary layers," Annu. Rev. Fluid Mech. **35**, 413 (2003).
[6] Y. B. Ma and X. L. Zhong, "Receptivity of a supersonic boundary layer over a flat plate. Part 3. Effects of different types of free-stream disturbances," J. Fluid Mech. **532**, 63 (2005).
[7] L. Mack, "Remarks on disputed numerical results in compressible boundary-layer stability theory," Phys. Fluids **27**, 342 (1984).
[8] A. Pagella, U. Rist, and S. Wagner, "Numerical investigations of small-amplitude disturbances in a boundary layer with impinging shock wave at Ma=4.8," Phys. Fluids **14**, 2088 (2002).
[9] P. Balakumar, H. W. Zhao, and H. Atkins, "Stability of hypersonic boundary layers over a compression corner," AIAA J. **43**, 760 (2005).
[10] T. Herbert, "Parabolized stability equations," Annu. Rev. Fluid Mech. **29**, 245 (1997).
[11] S. Hein, A. Stolte, and U. C. Dallmann, "Identification and analysis of nonlinear transition scenarios using NOLOT/PSE," Z. Angew. Math. Mech. **79**, S109(1999).
[12] D. Arnal and G. Casalis, "Laminar-turbulent transition prediction in three-

dimensional flows," Prog. Aerosp. Sci. **36**, 173 (2000).
[13]H. W. Stock, "e(N) transition prediction in three-dimensional boundary layers on inclined prolate spheroids," AIAA J. **44**, 108 (2006).
[14]L. Kleiser and T. A. Zang, "Numerical simulation of transition in wall-bounded shear flows," Annu. Rev. Fluid Mech. **23**, 495 (1991).
[15]A. Pagella, A. Babucke, and U. Rist, "Two-dimensional numerical investigations of small-amplitude disturbances in a boundary layer at Ma=4.8: Compression corner versus impinging shock wave," Phys. Fluids **16**, 2272 (2004).
[16]D. R. Chapman, D. M. Kuehn, and H. K. Larson, "Investigation of separated flows in supersonic and subsonic streams with emphasis on the effect of transition," NACA Report 1356, 1958.
[17]H. W. Zhao and P. Balakumar, "Nonlinear disturbance evolution across a hypersonic compression corner," AIAA J. **43**, 1034 (2005).
[18]S. Teramoto, "Large-eddy simulation of transitional boundary layer with impinging shock wave," AIAA J. **43**, 2354 (2005).
[19]M. Gerritsen and P. Olsson, "Designing an efficient solution strategy for fluid flows—A stable high order finite difference scheme and sharp shock resolution for the Euler equations," J. Comput. Phys. **129**, 245 (1996).
[20]H. C. Yee, N. D. Sandham, and M. J. Djomehri, "Low-dissipative high-order shock-capturing methods using characteristic-based filters," J. Comput. Phys. **150**, 199 (1999).
[21]N. D. Sandham, Q. Li, and H. C. Yee, "Entropy splitting for high-order numerical simulation of compressible turbulence," J. Comput. Phys. **178**, 307 (2002).
[22]M. H. Carpenter, J. Nordstrom, and D. Gottlieb, "A stable and conservative interface treatment of arbitrary spatial accuracy," J. Comput. Phys. **148**, 341 (1999).
[23]F. Ducros, V. Ferrand, F. Nicoud, C. Weber, D. Darracq, C. Gacherieu and T. Poinsot, "Large-eddy simulation of the shock turbulence interaction," J. Comput. Phys. **152**, 517 (1999).
[24]F. M. White, *Viscous Fluid Flow*, 2nd ed. (McGraw-Hill, New York, 1991).
[25]N. D. Sandham, Y. F. Yao, and A. A. Lawal, "Large-eddy simulation of transonic turbulent flow over a bump," Int. J. Heat Fluid Flow **24**, 584 (2003).
[26]L. Krishnan, Y. Yao, N. D. Sandham, and G. T. Roberts, "On the response of shock-induced separation bubble to small amplitude disturbances," Mod. Phys. Lett. B **19**, 1495 (2005).
[27]R. J. Hakkinen, I. Greber, L. Trilling, and S. S. Abarbanel, "The interaction of an oblique shock wave with a laminar boundary layer," NASA Memo 2-18-59W, 1959.
[28]E. Katzer, "On the lengthscales of laminar shock/boundary-layer interaction," J. Fluid Mech. **206**, 477 (1989).
[29]B. Wasistho, "Spatial direct numerical simulation of compressible boundary layer flow," Ph.D. thesis, University of Twente, Netherlands, 1998.
[30]R. D. Sandberg, "Numerical investigation of transitional and turbulent supersonic axisymmetric wakes," Ph.D. thesis, University of Arizona, 2004.
[31]E. Weibust, A. Bertelrud, and S. O. Ridder, "Experimental investigation of laminar separation bubbles and comparison with theory," J. Aircr. **24**, 291 (1987).
[32]M. Zhuang, "The effects of curvature on wake-dominated incompressible free shear layers," Phys. Fluids **11**, 3106 (1999).
[33]D. Papamoschou and A. Roshko, "The compressible turbulent shear-layer—an experimental study," J. Fluid Mech. **197**, 453 (1988).
[34]N. D. Sandham and W. C. Reynolds, "Three-dimensional simulations of large eddies in the compressible mixing layer," J. Fluid Mech. **224**, 133 (1991).
[35]M. M. Rai and P. Moin, "Direct numerical simulation of transition and turbulence in a spatially evolving boundary layers," J. Comput. Phys. **109**, 169 (1993).
[36]S. Pirozzoli, F. Grasso, and T. B. Gatski, "Direct numerical simulation and analysis of a spatially evolving supersonic turbulent boundary layer at M=2.25," Phys. Fluids **16**, 530 (2004).
[37]G. Simeonides and W. Haase, "Experimental and computational investigations of hypersonic flow about compression ramps." J. Fluid Mech. **283**, 17 (1995).